

GIBLy: Improving 3D Semantic Segmentation through an Architecture-Agnostic Lightweight Geometric Inductive Bias Layer

Diogo Lavado

NOVA School of Science and Technology, Portugal and
Università degli Studi di Milano, Italy

d.lavado@campus.fct.unl.pt

Alessandra Micheletti

Università degli Studi di Milano, Italy
alessandra.micheletti@unimi.it

Cláudia Soares

NOVA School of Science and Technology, Portugal

claudia.soares@fct.unl.pt

Abstract

*In 3D scene understanding, deep learning models rely on large models and extensive training to capture basic geometric structures that are present in the 3D data. However, existing methods lack explicit mechanisms to incorporate geometric information, such as learnable primitive shapes, often necessitating large models and more training data which in turn increases cost and can limit generalization. We introduce **GIBLy**, a lightweight geometric inductive bias layer that integrates learnable geometric priors into 3D segmentation pipelines. **GIBLy** enhances existing architectures – whether MLP-based, convolution-based, or transformer-based – by providing features aligned with simple geometric shapes (and thus human-interpretable) that improve segmentation performance with minimal computational overhead. We validate our approach across multiple 3D semantic segmentation benchmarks, demonstrating consistent performance gains, including up to **+11.5% mIoU on TS40K** with PTV3, while adding only **58K extra parameters**. Our results highlight the benefit of explicitly encoding geometric structure to support accurate and efficient 3D scene understanding, with a lightweight add-on layer*

1. Introduction

3D data is ubiquitous in applications such as autonomous driving, augmented reality, and robotics. Unlike images, which are organized on regular pixel grids, 3D point clouds lack the fixed pixel array structure: points are scattered in 3D space with varying density, so conventional image CNNs cannot be directly applied.

Current state-of-the-art methods in 3D scene understanding can be broadly categorized by their feature ex-

traction strategies. Early works like PointNet [35] and PointNet++ [36] employ shared multilayer perceptrons (MLPs) to extract features directly from raw point clouds. Convolution-based approaches, in contrast, leverage the convolution operator to capture both local and global context, either by rasterizing point clouds into volumetric grids [30, 31, 34] or by operating directly on the irregular point sets [27, 40, 47]. More recently, transformer-based architectures have emerged [16, 43, 48, 49, 56], exploiting attention mechanisms [41] to achieve superior point-wise feature extraction and overall performance. Nonetheless, these methods typically focus on learning geometric relationships implicitly from data, rather than incorporating explicit geometric priors that could guide feature extraction more directly. They rely on substantial computational resources, memory, and complex architectures to learn geometric relationships that are common across various tasks; e.g., a network might have to learn from scratch what a *flat surface* or *elongated cylinder* look like, which are concepts that could be built in as priors. For example, convolution-based methods benefit from built-in inductive biases such as locality and translation equivariance, which have enabled their success in image processing. In contrast, MLP-based methods, including vanilla transformer architectures, lack such inherent biases and must learn spatial relationships entirely from data. In 3D, we lack analogous built-in geometric biases for many architectures. This gap motivates techniques to integrate explicit geometric cues into existing 3D models. By augmenting a model with lightweight, interpretable geometric inductive biases (GIBs), one can enhance feature extraction without modifying the underlying architecture or adding significant computational cost.

To address these limitations, we introduce **GIBLy**, a lightweight geometric inductive bias layer that integrates learnable parametric geometric priors into 3D deep learn-

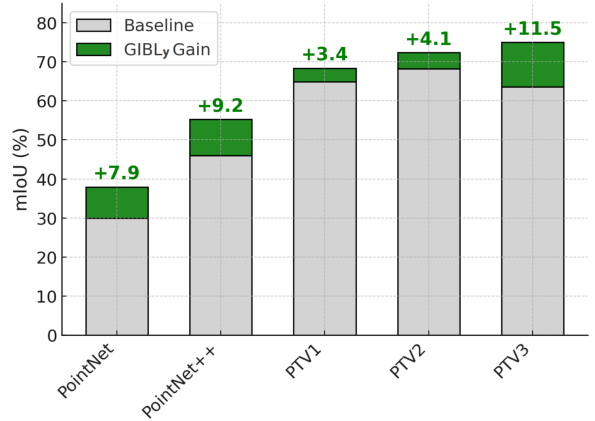
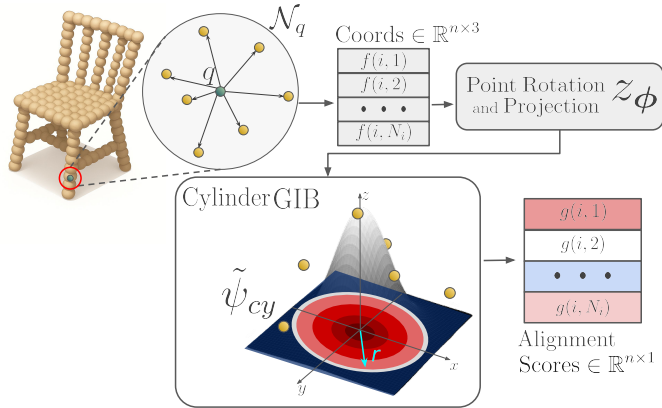


Figure 1. **GIBLy injects learnable geometric priors to improve 3D understanding.** *Left:* A Cylinder geometric inductive bias (GIB) aligns to a chair leg (neighborhood \mathcal{N}_q), using learned orientation ϕ and radius r , producing an alignment score. *Right:* On TS40K [21], adding a GIB-Layer (GIBLy) single-handedly boosts mIoU across multiple backbones (up to **+11.5%** mIoU on PTV3 [49]) with only **58K extra parameters**.

ing models. GIBLy is model-agnostic and can be integrated without altering the underlying architecture. This layer provides shape-aligned, interpretable features that enhance spatial reasoning without altering the underlying architecture or introducing significant computational overhead. We validate GIBLy through extensive experiments across diverse 3D semantic segmentation backbones [35, 36, 40, 48, 49, 56] and benchmarks [1, 3, 6, 10, 21]. Our results show that GIBLy improves performance, including a notable boost of +11.5% mIoU on TS40K [21] with Point-TransformerV3 [49], all while adding just **58K trainable parameters**. Our main contributions are:

- We introduce GIBLy, a geometric inductive bias layer that is lightweight, interpretable, and architecture-agnostic. It provides explicit geometric cues for 3D scene understanding and easily integrates into diverse 3D architecture.
- We demonstrate that GIBLy improves performance across a wide range of 3D segmentation models and benchmarks with minimal additional parameters and no modifications to the base architecture. Our model can improve mIoU by up to 10% with only 58K more parameters.
- We provide extensive ablation studies showing how the placement, neighborhood size, number of GIB instances, and bias types influence performance and efficiency.

2. Related Work

3D Scene Understanding. In 3D point cloud understanding, deep learning architectures are typically categorized into three paradigms based on their strategy to model point cloud data. Projection-based methods project 3D point clouds onto different 2D planes to utilize 2D CNN frameworks to infer 3D semantics [18, 23, 29, 38, 53]. Voxel-based methods discretize point clouds as voxel-grids to fa-

cilitate 3D convolutions [24, 30, 31, 55]. While effective, these voxel approaches face scalability issues; sparse convolution techniques subsequently alleviated this problem [8, 34, 44]. In turn, point-based methods retain the full detail of 3D point clouds by processing them directly [15, 27, 35, 36, 40]. Recent developments of the attention mechanism [41] tailored for point cloud processing have enabled new breakthroughs in performance and are gradually becoming dominant in most prominent benchmarks [16, 17, 33, 43, 48, 49, 56]. Nevertheless, attention mechanisms suffer from expensive calculation and memory footprint.

Convolution-based learning The lack of structure and irregular density of point clouds sharply contrast with the consistent frame of images. To circumvent this, projection- and voxel-based methods force point clouds into a structured and rasterized grid, allowing 2D and 3D CNN methods to be employed. However, 2D projections discard some geometric information of point clouds, and processing 3D voxel-grids incurs high computational and memory costs.

Graph convolutional networks in the spatial domain offer a natural alternative for feature extraction by interpreting point clouds as geometric graphs [14, 37]. These strategies are typically divided by the nature of their convolution kernels: discrete-kernel methods [25, 26, 40, 42, 57] follow standard CNN kernels and define filters on regular grids in the euclidean space, similar to 3D-CNN kernels for voxel-grids [30]. In turn, continuous-kernel methods [12, 27, 45, 47, 51] parameterize convolution as a function of local point coordinates. For instance, these techniques may represent the filter as $w = h(x_j - x_i)$, where h is a continuous function and x_j is a neighbor of x_i . Typically, h is expressed as a multi-layer perceptron (MLP) due

to their theoretical ability to approximate any continuous function. In this work, we augment the convolution kernel function h with a continuous parametric function that represents a geometric inductive bias. This geometric bias serves as an interpretable feature extractor, providing prior knowledge to the network and aiding convergence.

Geometric Informed Learning. Incorporating geometric information into neural networks has been extensively studied in learning-based surrogate models for solving partial differential equations (PDEs) in fluid dynamics [7, 28, 32], as well as in object generation using meshes [13] or enforcing shape constraints [4]. In point cloud processing, prior works [5, 19, 20] have leveraged geometric priors for various tasks. These methods demonstrate the benefit of geometric priors, but each is specific to a domain and not general-purpose, such as detecting protein pockets [5] and identifying power grid components [20]. In this work, we capitalize on the fact that 3D objects can often be described by basic geometric properties to develop a general-purpose geometric feature extractor model. Additionally, we demonstrate how integrating explicit geometric features into existing architectures can enhance performance across diverse tasks.

Inductive biases in 3D scene understanding. Inductive biases are essential for effective learning in computer vision. As formalized by the no-free-lunch theorem [2, 11], no model can generalize well across tasks without incorporating task-specific assumptions. In 3D scene understanding, geometric inductive biases are especially valuable due to the structured nature of real-world environments. Encoding these biases aligns the learning process with common geometric patterns, improving scene interpretation and reconstruction [54]. Convolutional networks benefit from built-in biases like locality and translation equivariance [9, 46], which support spatial structure learning. In contrast, MLPs lack such priors and must learn spatial relationships entirely from data. Augmenting MLPs with equivariant mechanisms has been shown to improve 3D understanding [39]. Similarly, transformer-based models exhibit inherent symmetries [22], and benefit from explicit geometric priors in applications such as depth estimation [52] and split training [50]. In this work, we incorporate geometric priors directly into existing 3D networks via GIBLy, a lightweight layer that improves performance without changes to the original network architecture.

3. Geometric Inductive Bias Layer

In this section we present the Geometric Inductive Bias Layer (GIBLy). The goal of GIBLy is to enrich 3D point features with explicit geometric structure while remaining lightweight and modular. First, we describe the general ar-

chitecture of the layer in Sec. 3.1. Next, we introduce a family of geometric inductive biases (GIBs) and their general form in Sec. 3.2. Lastly, we present the composition of GIBs into composite biases in Sec. 3.3.

Motivation. A central challenge in 3D scene understanding is that networks must learn geometric concepts directly from raw point clouds, which are irregular, sparse, and often incomplete. Unlike images, where convolutions benefit from built-in inductive biases, 3D backbones lack explicit geometric priors and must infer basic patterns (e.g., cylinders, planes) from data, often requiring large models and training. Yet, most objects can be decomposed into simple primitives: a table into a plane and four cylinders, or a car into an ellipsoid and narrow cylinders. While such structures recur across categories, their variation in design, scale, and shape makes fixed handcrafted priors too rigid [5, 19]. To address this, we propose GIBLy, a lightweight and modular layer that equips 3D backbones with learnable shape-aligned priors, injecting explicit geometric cues as point features at the input stage.

3.1. GIB-Layer (GIBLy)

GIBLy is designed to inject explicit, interpretable geometric structure into point features while being simple to integrate into existing backbones (Fig. 2). Each input point q is treated as a query, and multiple neighborhoods \mathcal{N}_q at different radii capture geometry across scales. Within each neighborhood, learnable geometric inductive biases (GIBs) measure the alignment of neighbors with primitives such as cylinders, cones, and disks, producing alignment scores $g(x)$. To move beyond simple shapes, GIBs are linearly combined into composite biases γ , enabling richer yet interpretable patterns. Learned coefficients weight the contribution of each primitive, highlighting which biases are most influential. The resulting geometric cues are concatenated with original point features, yielding enriched representations that can be processed by downstream modules. Crucially, GIBLy is applied only once at the input stage, where geometry is most reliable, enriched features are then propagated via skip connections through the network, avoiding repeated and less stable recomputation after downsampling.

3.2. Geometric Inductive Biases (GIBs)

GIBs on raw point clouds. To assess how well a neighborhood of points conforms to a geometric primitive, we require an operator capable of aggregating unordered local point sets and processing them with a tailored kernel. Point-based convolution naturally provides this functionality: it evaluates neighbors relative to a query point while allowing for the use of specialized kernels. Accordingly, geometric inductive biases (GIBs) can be integrated into raw point clouds by modeling them as geometric graphs and applying

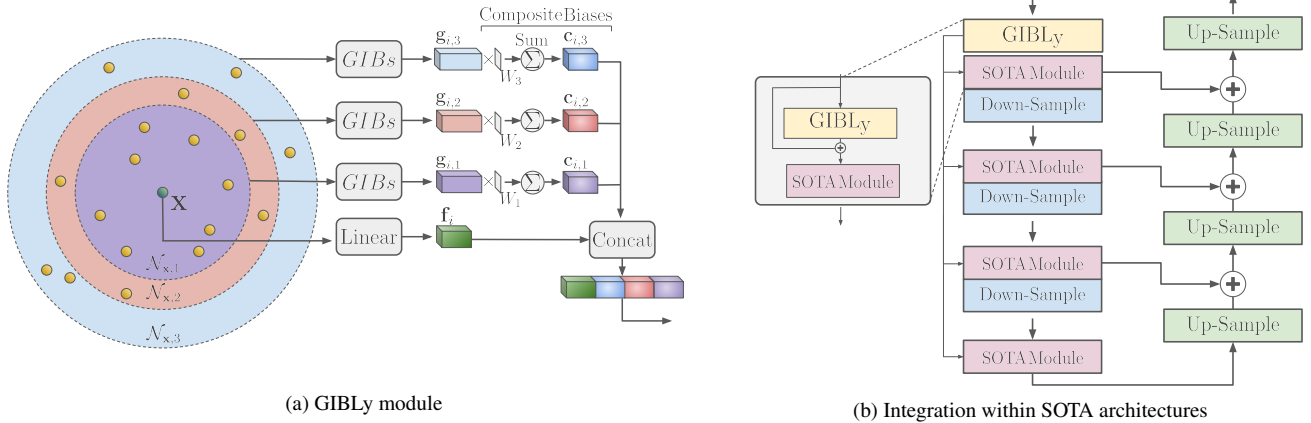


Figure 2. **Overview of our method.** (a) Our GIBLy module injects geometric awareness into point features by applying a set of learnable geometric inductive biases (GIBs) at each query point. We adopt a multi-region design: all input points are treated as query points, and multiple neighborhood scales are considered per point. For a given query i , $\mathbf{g}_{i,N}$ denotes the GIB alignment scores computed at N neighborhoods. These are linearly combined via learned weights W_N to produce composite bias responses $\mathbf{c}_{i,N}$, capturing richer geometric structure. The weights in W_N reflect the importance of each bias. The resulting features are concatenated with the original input features through MLPs or projection layers to produce enriched point representations. (b) GIBLy is applied once at the input level of a standard 3D backbone, where the geometry of the point cloud is most faithful. Its output features are propagated via skip connections to every downsampling stage in the encoder, allowing geometric information to be reused efficiently without reapplying the GIBLy module at every level.

point-based convolutions. This operator is particularly well suited for GIBs because it is translation-equivariant, ensuring that geometric features are detected independently of their absolute position in space.

GIBs as point-based convolutions. A raw point cloud is generally represented as $\mathcal{P} \in \mathbb{R}^{N \times (3+C)}$, where N is the number of points, and $3 + C$ denotes the spatial coordinates along with any additional point-wise features, such as color or intensity. Point-based continuous convolution treats \mathcal{P} as a sampling of an underlying continuous function $f: \mathbb{R}^3 \mapsto \mathbb{R}^C$, with a kernel function $g: \mathbb{R}^3 \mapsto \mathbb{R}$ given by:

$$(\mathcal{P} * g)(\mathbf{x}) = \int_{\mathbb{R}^3} g(\mathbf{y} - \mathbf{x}) f(\mathbf{y}) d\mathbf{y} \quad (1)$$

$$\approx \sum_{\mathbf{y} \in \mathcal{N}_{\mathbf{x}}} g(\mathbf{y} - \mathbf{x}) f(\mathbf{y}), \quad (2)$$

where $\mathcal{N}_{\mathbf{x}}$ denotes the local neighborhood of \mathbf{x} . Continuous-convolution approaches [27, 47, 51] typically approximate the kernel g using a multi-layer perceptron (MLP) due to its universal approximation theorem. However, such MLP-based methods must learn spatial relationships from data, which can increase model complexity, slow convergence, and reduce robustness to novel inputs. To alleviate these issues, we incorporate a family of continuous functions that provide alignment scores informed by geometric priors. Specifically, we parameterize g as:

$$g(\mathbf{z}) = \psi(\mathbf{z}; \eta), \quad (3)$$

where $\mathbf{z} = \mathbf{y} - \mathbf{x}$ represents the projection of a neighbor point \mathbf{y} onto a canonical reference space, ψ is a geometric basis function (e.g. radial basis function) that encodes specific shape attributes, with η serving as a learnable parameter that defines these shape characteristics (e.g., the radius of a cylinder). This formulation enables the network to efficiently capture and utilize geometric structures while preserving a transparent interpretation of the shape parameters η .

Designing GIBs. Each GIB is implemented as a radial basis function (RBF) defined in terms of the relative position of neighboring points. Specifically, given a query point q and its local neighborhood \mathcal{N}_q , we define the position of each neighbor $x \in \mathcal{N}_q$ relative to q (i.e., we center each neighbor at the query point). This relative vector is then rotated by a learnable rotation matrix R_ϕ and projected into a reference space:

$$z_\phi(x) = z(R_\phi^\top(x - q)), \quad g(x) = \psi_g(z_\phi(x); \eta), \quad (4)$$

where ψ_g is a geometric kernel (e.g., Gaussian), $\phi = [\phi_x, \phi_y, \phi_z]$ are learned rotation angles, and η are shape parameters (e.g., radius, thickness). The vector ϕ explicitly parametrizes the rotation matrix R_ϕ , enabling the model to learn a rotation that aligns the relative neighbor coordinates with the GIB ψ_g , thus providing a learnable rotation equivariance per GIB instead of enforcing a predefined rotation equivariance. Consequently, this learned rotation

effectively orients the geometric cues encoded by ψ_g , allowing the GIB to adapt to different local geometric configurations. The output $g(x)$ denotes the alignment score of the neighbor x with respect to the geometric prior centered on q . Real-world objects seldom adhere to strict geometric forms, making fixed boundaries unsuitable for capturing their variability. Thus, RBFs offer a continuous similarity measure between points in a local neighborhood and the encoded geometric priors. This enables a more adaptive representation of natural structures without enforcing hard constraints. We selected the primitives cylinders, cones, planes/disks, ellipsoids as basic components to common structures in man-made and natural environments, such as columns, slopes, and blobs. We now introduce the Cylinder GIB and its hollowed variant, which serve as representative examples of our geometric bias formulation. To avoid repetition, detailed definitions of the remaining GIB types, including cones, disks, and ellipsoids, are provided in the Supplementary Material.

Cylinder GIB. The Cylinder GIB models long, tubular structures that are common in both indoor (e.g., table legs, poles) and outdoor (e.g., tree trunks, signposts) scenes. It uses a Gaussian function centered on a cylindrical axis, favoring radial symmetry around a central spine:

$$\psi_{cy}(x) = \exp\left(-\frac{\|z_\phi(x)\|^2}{2r^2}\right) \quad (5)$$

Here, $z_\phi(x)$ represents the projection of point x into a canonical coordinate system defined by the learned rotation matrix R_ϕ , which aligns the cylinder with relevant features in the scene. The term $\|z_\phi(x)\|$ corresponds to the radial distance from the cylinder’s central axis. The parameter r defines the cylinder radius and controls the spread of the Gaussian kernel. Points close to the axis receive high alignment scores, while those farther away are suppressed. The shape parameters for this GIB are $\eta_{cy} = [r, \phi]$ and a depiction of these operations can be found in Fig. 1 on the left.

Hollow Cylinder GIB. In many real-world scenarios, especially with LiDAR or RGB-D data, cylindrical structures may exhibit hollow interiors due to surface-only sampling. Examples include pipes, cables, or hollow rods. To model these shell-like geometries, we define the Hollow Cylinder GIB:

$$\psi_{hcy}(x) = \exp\left(-\frac{(\|z_\phi(x)\| - r)^2}{2t^2}\right) \quad (6)$$

Unlike the standard cylinder, this function peaks at a fixed distance r from the axis, suppressing the core and exterior. The parameter t controls the shell thickness, effectively defining the tolerance band around the ring. The shape parameters are extended to $\eta_{hcy} = [r, t, \phi]$.

GIB normalization. Similar to batch normalization layers in convolution-based architectures, we propose a normalization operation for geometric inductive biases. In conventional CNNs, batch normalization is applied directly to the feature maps produced by convolutional layers to standardize their distributions across a mini-batch. However, due to the distinct nature of GIB modules, a direct application of batch normalization is not feasible seeing as it could invert the semantics of alignment scores (i.e., assigning negative values to geometrically aligned neighbors and positive values to misaligned ones). For a given GIB instance ψ , its score over a local neighborhood \mathcal{N}_q quantifies the degree to which each neighbor is aligned with the geometric pattern encoded by ψ . Consequently, the normalized bias, denoted by $\tilde{\psi}$, is designed to yield positive values for neighbors that conform to the desired geometric configuration and negative values for those that deviate. This normalization not only ensures that the alignment scores are on a comparable scale across different neighborhoods but also reinforces the intended geometric characteristics while suppressing spurious or misaligned shapes. To this end, we employ a Monte Carlo approximation to estimate the integral of ψ over the neighborhood domain \mathcal{N}_q . Specifically, we define the cumulative alignment score as:

$$\Omega(x) = \int_{\mathcal{N}_q} \psi(y) dy \approx \sum_{y \in \mathcal{MC}} \psi(y). \quad (7)$$

Here, the set $\mathcal{MC} = \{y \in \mathbb{R}^3 \mid \|y\| \leq r\}$ serves as a Monte Carlo approximation of the neighborhood \mathcal{N}_q , where r denotes the neighborhood’s radius. The normalized GIB is computed by subtracting the average alignment over the neighborhood from the original score:

$$\tilde{\psi}(x) = \psi(x) - \frac{\Omega(x)}{|\mathcal{MC}|}. \quad (8)$$

Normalizing GIBs is essential for robustly integrating geometric cues into deep learning frameworks. This operation is illustrated in Fig. 3.

3.3. Composite Biases

Although geometric inductive biases (GIBs) offer several degrees of freedom via their shape parameters η to adapt to input data, a single GIB may be insufficient to capture the intricate details inherent in sophisticated objects. To address this limitation, we propose a framework in which multiple GIB instances are combined into composite biases through linear combinations. Specifically, let $\Psi = \{\psi_j\}_{j=1}^m$ denote a set of m GIBs, where each instance ψ_j is selected from a parametric family belonging to $\{\psi_{cy}, \psi_{cn}, \psi_{ellip}, \psi_{dk}, \psi_{hcy}, \psi_{hcn}, \psi_{hellip}, \psi_{hdk}\}$. These biases are aggregated via a linear combination with a learnable weight matrix $W \in \mathbb{R}^{n \times m}$, where n is the number of

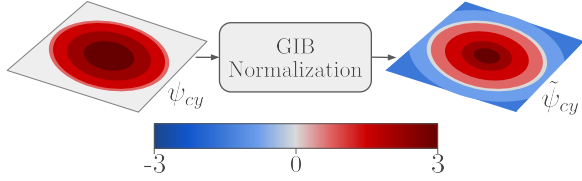


Figure 3. A normalized bias ensures that neighbors aligning with the desired geometric configuration receive positive values, while those deviating receive negative values. Here, a Cylinder GIB is normalized such that neighbor points receive an alignment score congruent with their proximity to the center. Once the radius is exceeded, points fall outside the geometric bias and receive negative scores, indicating deviation from the intended shape.

composite biases, collected in the set $\Gamma = \{\gamma_i\}_{i=1}^n$. Formally, each composite bias is defined as

$$\gamma_i = \sum_{\psi_j \in \Psi} W_{ij} \psi_j. \quad (9)$$

In this formulation, each row W_i quantifies the contribution of the individual GIBs to the composite bias γ_i . A positive coefficient W_{ij} indicates that the corresponding GIB ψ_j contributes constructively, activating the detection of specific patterns within the scene. In contrast, a negative coefficient implies that ψ_j exerts a suppressive influence, either altering the resulting shape or diminishing the detection of certain features. Moreover, the absolute value $|W_{ij}|$ serves as an indicator of the intensity and contribution of the j -th inductive bias within the model. A larger magnitude indicates that the model assigns greater importance to that GIB instance in forming the feature representation. It is important to note that this linear combination approach may introduce unwanted noise into composite biases, due to residual contributions from GIBs that are not pertinent to a particular composite γ_i . To mitigate this issue, we promote sparsity in the weight matrix by employing an L_1 penalty, and further regulate the overall magnitude of the weights through an L_2 penalty to prevent overfitting.

4. Experiments

4.1. Implementation Details

Baselines. We conducted experiments integrating our proposed GIBLy method into several 3D learning pipelines, including the seminal MLP-based methods PointNet [35] and PointNet++ [36] (in Supplementary Material), the convolution-based method KPConv [40], and the transformer-based PointTransformer architectures [48, 49, 56]. GIBLy was evaluated on standard benchmarks for indoor and outdoor 3D semantic segmentation. For indoor scene understanding, we consider ScanNet v2 [10] and the S3DIS dataset [1]. For outdoor

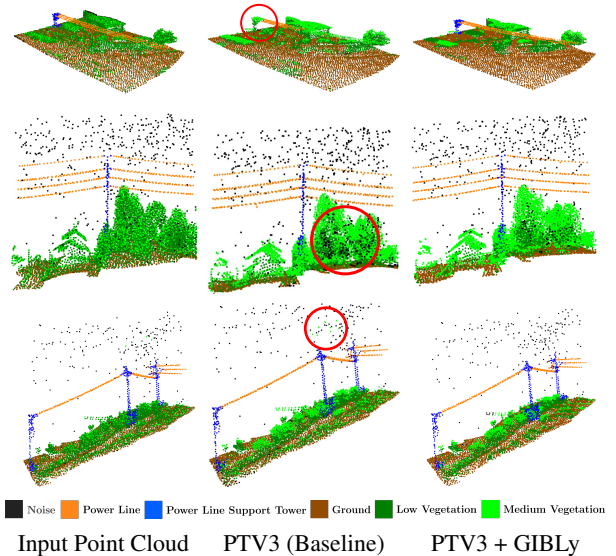


Figure 4. **Qualitative results on the TS40K dataset.** Each row presents a different scene. From left to right: input point cloud, prediction from the baseline PointTransformerV3 (PTV3), and prediction from PTV3 augmented with GIBLy. In the three rows, the baseline fails to detect support towers, introduces spurious noise in vegetation regions, or misclassifies artifacts as vegetation. In contrast, the GIBLy-augmented model avoids these errors, producing more geometrically consistent predictions. Full view in Supplementary material.

scene segmentation, we evaluate on three benchmarks: nuScenes [6], SemanticKITTI [3], and TS40K [21]. While we evaluate across all datasets, we adopt TS40K as our primary benchmark for ablations and analysis. Unlike driving datasets, TS40K provides high-resolution LiDAR scans with dense sampling, no occlusion, and anisotropic point distributions within the same object. These properties allow neighborhoods to be reliably estimated and make geometric effects more directly observable, which is essential for isolating the contribution of GIBLy. The dataset also contains objects with strong global structure but diverse local variations (e.g., power line towers), which aligns well with the strengths of radial basis functions in capturing smooth global alignment while tolerating some local variation. Importantly, TS40K’s released configurations allowed us to reproduce baselines faithfully, enabling controlled and reproducible ablation studies.

4.2. Evaluation

TS40K. Table 1 presents the per-class and mean IoU results on the TS40K [21] dataset. We observe that GIBLy consistently improves performance across all backbones. The largest gains are observed for transformer models, with PTV3 [49] improving from 63.55% to 75.03% mIoU

Table 1. Semantic segmentation results on TS40K. GIBLy improves class-wise and mean IoU across most backbones. Gains are shown in green and deficits in red.

Method		mIoU (%)	Noise	Ground	Low Veg.	Mid Veg.	Tower	Power Line
KPCConv	base	52.77	57.02	64.75	37.12	34.63	37.36	89.99
	+ GIBLy	46.83	53.37	61.96	35.73	31.26	12.91	85.78
	Δ	-5.94	-3.65	-2.79	-1.39	-3.37	-24.45	-4.21
PTV1	base	64.90	57.50	77.33	60.34	46.51	54.19	93.54
	+ GIBLy	68.33	63.88	79.15	68.77	50.93	52.16	95.06
	Δ	+3.43	+6.38	+1.82	+8.43	+4.42	-2.03	+1.52
PTV2	base	68.29	61.16	80.13	68.17	51.39	54.48	94.43
	+ GIBLy	72.35	67.79	82.40	73.17	54.38	60.29	96.06
	Δ	+4.06	+6.63	+2.27	+5.00	+2.99	+5.81	+1.63
PTV3	base	63.55	59.23	70.77	50.47	43.86	61.42	95.53
	+ GIBLy	75.03	68.91	82.96	73.32	55.33	72.49	97.17
	Δ	+11.48	+9.68	+12.19	+22.85	+11.47	+11.07	+1.64

Table 2. Semantic segmentation results (mIoU %) and improvements (Δ) across four benchmarks.¹ Gains are shown in green and deficits in red.

Method		nuScenes		SemanticKITTI		ScanNet v2		S3DIS (Area 5)	
		mIoU	Δ	mIoU	Δ	mIoU	Δ	mIoU	Δ
KPCConv	base	50.74	-	45.24	-	36.95	-	30.31	-
	+ GIBLy	37.33	-13.41	47.55	+2.31	29.46	-7.49	35.71	+5.40
PTV1	base	66.29	-	50.17	-	33.16	-	47.14	-
	+ GIBLy	54.38	-11.91	53.70	+3.53	39.08	+5.92	51.14	+4.00
PTV2	base	65.40	-	54.15	-	52.05	-	56.42	-
	+ GIBLy	70.26	+4.86	55.88	+1.73	55.27	+3.22	65.10	+8.68
PTV3	base	74.20	-	55.09	-	55.64	-	60.44	-
	+ GIBLy	69.91	-4.29	58.14	+3.05	57.79	+2.15	67.96	+7.52

¹ For fair evaluation, all models are trained under the same conditions without the use of additional training data or benchmark-specific augmentation pipelines. Some methods (e.g., PTV3 [49]) report higher performance using extra data. We instead report performance under a controlled and equal setting to ensure valid comparison between each backbone and its GIBLy-augmented variant. Training configurations are fully described in Supplementary Material.

(+11.48). The increase is also notable for lightweight MLPs like PointNet, which gains 7.95 mIoU. However, KPConv [40] shows small regressions, which we attribute to incompatibility between rigid grid-based kernels and soft geometric biases.

nuScenes, SemanticKITTI, ScanNet v2, and S3DIS.

Table 2 shows consistent gains across most backbones and datasets. Improvements are especially strong on S3DIS [1], with boosts of +7.52% (PTV3 [49]) and +8.68% (PTV2 [48]), confirming GIBLy’s effectiveness in structured indoor scenes. SemanticKITTI [3] also benefits, particularly for PointTransformer models, with up to +3.53% gain on PTV1 [56]. In ScanNet v2 [10], GIBLy improves all PointTransformer variants, while PointNet-based

models [35, 36] degrade likely due to limited feature capacity. Performance on nuScenes [6] varies: while PointNet, PointNet++ and PTV2 improve, KPConv [40], PTV1, and PTV3 underperform. We do not claim new state-of-the-art performance on these benchmarks but demonstrate consistent improvements across strong backbones. Although our reproduced baselines do not reach the exact performance reported in the original papers, GIBLy consistently improves upon them with exactly the same training setting.

4.3. Ablation Study

We conduct ablations on the TS40K validation set to evaluate the impact of key GIBLy design choices, including placement strategy, neighborhood count, normalization, composite biases, number of GIBs, and bias type, with addi-

Table 3. Ablation on GIBLy placement strategy.

Configuration	mIoU (%)	Δ (%)
Baseline (PTV3)	65.80	
GIBLy (input only (default))	75.94	+10.14
GIBLy (input + intermediate)	66.18	+0.38
GIBLy (every stage)	56.41	-9.39

Table 4. Ablation on the number of GIB neighborhood levels.

# Neighborhoods	mIoU (%)	Latency (ms)
1	69.12	23.1
2	72.41	29.2
3 (default)	75.94	37.0
5	68.56	50.4

Table 5. Ablation on the number of GIB instances per layer.

GIBs per Prior	mIoU (%)	Latency (ms)
2 (default)	75.94	27.0
4	73.92	32.6
8	71.67	39.2
16	68.84	42.4

tional studies provided in the Supplementary Material. All experiments use PTV3 [49] as the backbone.

GIBLy Placement. As shown in Table 3, placing a single GIBLy layer at the input stage achieves the best performance, improving by +10.14 mIoU over the baseline. Adding GIBLy at intermediate stages brings limited additional benefit. Interestingly, placing GIBLy layers at every stage leads to a noticeable drop of -9.39 mIoU. We attribute this degradation to the loss of geometric detail with the use of downsampling at deeper levels.

Neighborhood Count. In Table 4, we evaluate how the number of neighborhood levels affects segmentation accuracy and computational overhead. A single neighborhood radius yields lower performance, while increasing the number of radii improves accuracy up to a point. Using 2 or 3 neighborhoods achieves the best trade-off between accuracy and latency.

Number of GIBs. In Table 5, we vary the number of GIB instances per layer to study their impact on accuracy and runtime. Using two GIBs per shape achieves the best result. Increasing the number beyond this leads to negative returns.

Bias Shape Variants. In Table 6, we isolate the impact of different GIB families. Using the full set of biases outperforms any subset, with radial-only or hollow-only GIBs

showing moderate performance. Ellipsoid biases in isolation yield the lowest performance, showing the benefit of combining different priors.

Table 6. Ablation on geometric bias types.

Bias Types	mIoU (%)	Δ (%)
Radial only (cylinder, disk)	71.14	-4.80
Hollow only	71.30	-4.64
Ellipsoid only	68.42	-7.52
All GIBs (default)	75.94	

Composite Biases. In Table 7, we evaluate the role of composite biases. Using none severely limits performance, while increasing their number progressively improves results up to 16 composites. Beyond this point, performance saturates and slightly decreases, suggesting that a moderate number of composites provides the best balance between expressiveness and overfitting.

Table 7. Ablation on composite biases.

Number of Composites	mIoU (%)
0	59.60
2	66.06
4	69.33
8	72.14
16 (default)	75.94
64	73.75
128	72.57

GIB Normalization. Table 8 shows the impact of normalization. Without normalization, performance drops significantly as alignment scores are dominated by neighborhood density. Standard z-score normalization partially recovers performance but produces inconsistent semantics, since well-aligned neighbors may be assigned negative values. Our proposed normalization yields the best results, confirming its importance for stable integration of GIBs.

5. Conclusions

In this paper we present GIBLy, a geometric inductive bias layer that integrates lightweight, learnable geometric priors into existing 3D learning models. GIBLy is model-agnostic and can be integrated without altering the underlying architecture. By explicitly encoding shape-aware information, GIBLy increases the performance of the majority of baseline models with only 58K extra parameters and a single layer at the input stage. As for limitations, GIBLy relies on predefined geometric templates that, while expressive,

Table 8. Ablation on GIB normalization.

Normalization Type	mIoU (%)
No Normalization	62.92
Standardization	67.84
GIB Normalization (default)	75.94

may not capture irregular structures. An exciting direction for future work is to extend GIBLy with data-driven biases beyond simple primitives with more degrees of freedom.

References

- [1] Iro Armeni, Ozan Sener, Amir R Zamir, Helen Jiang, Ioannis Brilakis, Martin Fischer, and Silvio Savarese. 3d semantic parsing of large-scale indoor spaces. In *Proceedings of the IEEE conference on computer vision and pattern recognition*, pages 1534–1543, 2016. 2, 6, 7
- [2] Jonathan Baxter. A model of inductive bias learning. *Journal of artificial intelligence research*, 12:149–198, 2000. 3
- [3] Jens Behley, Martin Garbade, Andres Milioto, Jan Quenzel, Sven Behnke, Cyrill Stachniss, and Jurgen Gall. Semantickitti: A dataset for semantic scene understanding of lidar sequences. In *Proceedings of the IEEE/CVF international conference on computer vision*, pages 9297–9307, 2019. 2, 6, 7
- [4] Arturs Berzins, Andreas Radler, Eric Volkmann, Sebastian Sanokowski, Sepp Hochreiter, and Johannes Brandstetter. Geometry-informed neural networks. *arXiv preprint arXiv:2402.14009*, 2024. 3
- [5] Giovanni Bocchi, Patrizio Frosini, Alessandra Micheletti, Alessandro Pedretti, Carmen Gratteri, Filippo Lunghini, Andrea Rosario Beccari, and Carmine Talarico. Geneonet: A new machine learning paradigm based on group equivariant non-expansive operators. an application to protein pocket detection. *arXiv preprint arXiv:2202.00451*, 2022. 3
- [6] Holger Caesar, Varun Bankiti, Alex H Lang, Sourabh Vora, Venice Erin Liong, Qiang Xu, Anush Krishnan, Yu Pan, Giancarlo Baldan, and Oscar Beijbom. nuscenes: A multi-modal dataset for autonomous driving. In *Proceedings of the IEEE/CVF conference on computer vision and pattern recognition*, pages 11621–11631, 2020. 2, 6, 7
- [7] Scott Cameron, Arnu Pretorius, and Stephen Roberts. Non-parametric boundary geometry in physics informed deep learning. *Advances in Neural Information Processing Systems*, 36, 2024. 3
- [8] Christopher Choy, JunYoung Gwak, and Silvio Savarese. 4d spatio-temporal convnets: Minkowski convolutional neural networks. In *Proceedings of the IEEE/CVF conference on computer vision and pattern recognition*, pages 3075–3084, 2019. 2
- [9] Nadav Cohen and Amnon Shashua. Inductive bias of deep convolutional networks through pooling geometry. *arXiv preprint arXiv:1605.06743*, 2016. 3
- [10] Angela Dai, Angel X Chang, Manolis Savva, Maciej Halber, Thomas Funkhouser, and Matthias Nießner. Scannet: Richly-annotated 3d reconstructions of indoor scenes. In *Proceedings of the IEEE conference on computer vision and pattern recognition*, pages 5828–5839, 2017. 2, 6, 7
- [11] Anirudh Goyal and Yoshua Bengio. Inductive biases for deep learning of higher-level cognition. *Proceedings of the Royal Society A*, 478(2266):20210068, 2022. 3
- [12] Fabian Groh, Patrick Wieschollek, and Hendrik PA Lensch. Flex-convolution: Million-scale point-cloud learning beyond grid-worlds. In *Asian Conference on Computer Vision*, pages 105–122. Springer, 2018. 2
- [13] Rana Hanocka, Amir Hertz, Noa Fish, Raja Giryes, Shachar Fleishman, and Daniel Cohen-Or. Meshcnn: a network with an edge. *ACM Transactions on Graphics (TOG)*, 38(4):1–12, 2019. 3
- [14] Pedro Hermosilla, Tobias Ritschel, Pere-Pau Vázquez, Àlvar Vinacua, and Timo Ropinski. Monte carlo convolution for learning on non-uniformly sampled point clouds. *ACM Transactions On Graphics (TOG)*, 37(6):1–12, 2018. 2
- [15] Lingdong Kong, Youquan Liu, Runnan Chen, Yuexin Ma, Xinge Zhu, Yikang Li, Yuenan Hou, Yu Qiao, and Ziwei Liu. Rethinking range view representation for lidar segmentation. In *Proceedings of the IEEE/CVF International Conference on Computer Vision*, pages 228–240, 2023. 2
- [16] Xin Lai, Jianhui Liu, Li Jiang, Liwei Wang, Hengshuang Zhao, Shu Liu, Xiaojuan Qi, and Jiaya Jia. Stratified transformer for 3d point cloud segmentation. In *Proceedings of the IEEE/CVF conference on computer vision and pattern recognition*, pages 8500–8509, 2022. 1, 2
- [17] Xin Lai, Yukang Chen, Fanbin Lu, Jianhui Liu, and Jiaya Jia. Spherical transformer for lidar-based 3d recognition. In *Proceedings of the IEEE/CVF Conference on Computer Vision and Pattern Recognition*, pages 17545–17555, 2023. 2
- [18] Alex H Lang, Sourabh Vora, Holger Caesar, Lubing Zhou, Jiong Yang, and Oscar Beijbom. Pointpillars: Fast encoders for object detection from point clouds. In *Proceedings of the IEEE/CVF conference on computer vision and pattern recognition*, pages 12697–12705, 2019. 2
- [19] Diogo Lavado, Cláudia Soares, Alessandra Micheletti, Giovanni Bocchi, Alex Coronati, Manuel Silva, and Patrizio Frosini. Low-resource white-box semantic segmentation of supporting towers on 3d point clouds via signature shape identification. *arXiv preprint arXiv:2306.07809*, 2023. 3
- [20] Diogo Lavado, Cláudia Soares, Alessandra Micheletti, et al. Scene-net v2: Interpretable multiclass 3d scene understanding with geometric priors. *PROCEEDINGS OF MACHINE LEARNING RESEARCH*, 251:222–232, 2024. 3
- [21] Diogo Lavado, Ricardo Santos, André Coelho, João Santos, Alessandra Micheletti, and Claudia Soares. Learning under noisy labels, spurious points, and diverse structures: Ts40k, a 3d point cloud dataset of rural terrain and electrical transmission systems. In *2025 IEEE/CVF Winter Conference on Applications of Computer Vision (WACV)*, pages 7326–7336. IEEE, 2025. 2, 6
- [22] Itay Lavie, Guy Gur-Ari, and Zohar Ringel. Towards understanding inductive bias in transformers: A view from infinity. In *Proceedings of the 41st International Conference on Machine Learning*, pages 26043–26069. PMLR, 2024. 3

- [23] Felix Järeemo Lawin, Martin Danelljan, Patrik Tosteberg, Goutam Bhat, Fahad Shahbaz Khan, and Michael Felsberg. Deep projective 3d semantic segmentation. In *Computer Analysis of Images and Patterns: 17th International Conference, CAIP 2017, Ystad, Sweden, August 22-24, 2017, Proceedings, Part I 17*, pages 95–107. Springer, 2017. 2
- [24] Truc Le and Ye Duan. Pointgrid: A deep network for 3d shape understanding. In *Proceedings of the IEEE conference on computer vision and pattern recognition*, pages 9204–9214, 2018. 2
- [25] Huan Lei, Naveed Akhtar, and Ajmal Mian. Octree guided cnn with spherical kernels for 3d point clouds. In *Proceedings of the IEEE/CVF Conference on Computer Vision and Pattern Recognition*, pages 9631–9640, 2019. 2
- [26] Huan Lei, Naveed Akhtar, and Ajmal Mian. Spherical kernel for efficient graph convolution on 3d point clouds. *IEEE transactions on pattern analysis and machine intelligence*, 43(10):3664–3680, 2020. 2
- [27] Yangyan Li, Rui Bu, Mingchao Sun, Wei Wu, Xinhan Di, and Baoquan Chen. Pointcnn: Convolution on x-transformed points. *Advances in neural information processing systems*, 31, 2018. 1, 2, 4
- [28] Zongyi Li, Nikola Kovachki, Chris Choy, Boyi Li, Jean Kossaifi, Shourya Otta, Mohammad Amin Nabian, Maximilian Stadler, Christian Hundt, Kamyar Azizzadenesheli, et al. Geometry-informed neural operator for large-scale 3d pdes. *Advances in Neural Information Processing Systems*, 36, 2024. 3
- [29] Yecheng Lyu, Xinming Huang, and Ziming Zhang. Learning to segment 3d point clouds in 2d image space. In *Proceedings of the IEEE/CVF Conference on Computer Vision and Pattern Recognition*, pages 12255–12264, 2020. 2
- [30] Daniel Maturana and Sebastian Scherer. Voxnet: A 3d convolutional neural network for real-time object recognition. In *2015 IEEE/RSJ international conference on intelligent robots and systems (IROS)*, pages 922–928. IEEE, 2015. 1, 2
- [31] Hsien-Yu Meng, Lin Gao, Yu-Kun Lai, and Dinesh Manocha. Vv-net: Voxel vae net with group convolutions for point cloud segmentation. In *Proceedings of the IEEE/CVF international conference on computer vision*, pages 8500–8508, 2019. 1, 2
- [32] Jan Oldenburg, Finja Borowski, Alper Öner, Klaus-Peter Schmitz, and Michael Stiehm. Geometry aware physics informed neural network surrogate for solving navier–stokes equation (gapinn). *Advanced Modeling and Simulation in Engineering Sciences*, 9(1):8, 2022. 3
- [33] Chunghyun Park, Yoonwoo Jeong, Minsu Cho, and Jaesik Park. Fast point transformer. In *Proceedings of the IEEE/CVF conference on computer vision and pattern recognition*, pages 16949–16958, 2022. 2
- [34] Bohao Peng, Xiaoyang Wu, Li Jiang, Yukang Chen, Hengshuang Zhao, Zhuotao Tian, and Jiaya Jia. Oa-cnns: Omni-adaptive sparse cnns for 3d semantic segmentation. In *Proceedings of the IEEE/CVF Conference on Computer Vision and Pattern Recognition*, pages 21305–21315, 2024. 1, 2
- [35] Charles R Qi, Hao Su, Kaichun Mo, and Leonidas J Guibas. Pointnet: Deep learning on point sets for 3d classification and segmentation. In *Proceedings of the IEEE conference on computer vision and pattern recognition*, pages 652–660, 2017. 1, 2, 6, 7
- [36] Charles Ruizhongtai Qi, Li Yi, Hao Su, and Leonidas J Guibas. Pointnet++: Deep hierarchical feature learning on point sets in a metric space. *Advances in neural information processing systems*, 30, 2017. 1, 2, 6, 7
- [37] Martin Simonovsky and Nikos Komodakis. Dynamic edge-conditioned filters in convolutional neural networks on graphs. In *Proceedings of the IEEE conference on computer vision and pattern recognition*, pages 3693–3702, 2017. 2
- [38] Hang Su, Subhransu Maji, Evangelos Kalogerakis, and Erik Learned-Miller. Multi-view convolutional neural networks for 3d shape recognition. In *Proceedings of the IEEE international conference on computer vision*, pages 945–953, 2015. 2
- [39] Weiwei Sun, Andrea Tagliasacchi, Boyang Deng, Sara Sabour, Soroosh Yazdani, Geoffrey E Hinton, and Kwang Moo Yi. Canonical capsules: Self-supervised capsules in canonical pose. *Advances in Neural information processing systems*, 34:24993–25005, 2021. 3
- [40] Hugues Thomas, Charles R Qi, Jean-Emmanuel Deschaud, Beatriz Marcotequi, François Goulette, and Leonidas J Guibas. Kpconv: Flexible and deformable convolution for point clouds. In *Proceedings of the IEEE/CVF international conference on computer vision*, pages 6411–6420, 2019. 1, 2, 6, 7
- [41] A Vaswani. Attention is all you need. *Advances in Neural Information Processing Systems*, 2017. 1, 2
- [42] Lei Wang, Yuchun Huang, Yaolin Hou, Shenman Zhang, and Jie Shan. Graph attention convolution for point cloud semantic segmentation. In *Proceedings of the IEEE/CVF conference on computer vision and pattern recognition*, pages 10296–10305, 2019. 2
- [43] Peng-Shuai Wang. Octformer: Octree-based transformers for 3d point clouds. *ACM Transactions on Graphics (TOG)*, 42(4):1–11, 2023. 1, 2
- [44] Peng-Shuai Wang, Yang Liu, Yu-Xiao Guo, Chun-Yu Sun, and Xin Tong. O-cnn: Octree-based convolutional neural networks for 3d shape analysis. *ACM Transactions On Graphics (TOG)*, 36(4):1–11, 2017. 2
- [45] Shenlong Wang, Simon Suo, Wei-Chiu Ma, Andrei Pokrovsky, and Raquel Urtasun. Deep parametric continuous convolutional neural networks. In *Proceedings of the IEEE conference on computer vision and pattern recognition*, pages 2589–2597, 2018. 2
- [46] Zihao Wang and Lei Wu. Theoretical analysis of the inductive biases in deep convolutional networks. *Advances in Neural Information Processing Systems*, 36:74289–74338, 2023. 3
- [47] Wenxuan Wu, Zhongang Qi, and Li Fuxin. Pointconv: Deep convolutional networks on 3d point clouds. In *Proceedings of the IEEE/CVF Conference on computer vision and pattern recognition*, pages 9621–9630, 2019. 1, 2, 4
- [48] Xiaoyang Wu, Yixing Lao, Li Jiang, Xihui Liu, and Hengshuang Zhao. Point transformer v2: Grouped vector attention and partition-based pooling. In *NeurIPS*, 2022. 1, 2, 6, 7

- [49] Xiaoyang Wu, Li Jiang, Peng-Shuai Wang, Zhijian Liu, Xihui Liu, Yu Qiao, Wanli Ouyang, Tong He, and Hengshuang Zhao. Point transformer v3: Simpler faster stronger. In *Proceedings of the IEEE/CVF Conference on Computer Vision and Pattern Recognition*, pages 4840–4851, 2024. [1](#), [2](#), [6](#), [7](#), [8](#)
- [50] Hengyuan Xu, Liyao Xiang, Hangyu Ye, Dixi Yao, Pengzhi Chu, and Baochun Li. Permutation equivariance of transformers and its applications. In *Proceedings of the IEEE/CVF Conference on Computer Vision and Pattern Recognition*, pages 5987–5996, 2024. [3](#)
- [51] Yifan Xu, Tianqi Fan, Mingye Xu, Long Zeng, and Yu Qiao. Spidercnn: Deep learning on point sets with parameterized convolutional filters. In *Proceedings of the European conference on computer vision (ECCV)*, pages 87–102, 2018. [2](#), [4](#)
- [52] Yinshuang Xu, Jiahui Lei, and Kostas Daniilidis. S^3 equivariant convolution and transformer in ray space. In *Thirty-seventh Conference on Neural Information Processing Systems*, 2023. [3](#)
- [53] Ze Yang and Liwei Wang. Learning relationships for multi-view 3d object recognition. In *Proceedings of the IEEE/CVF international conference on computer vision*, pages 7505–7514, 2019. [2](#)
- [54] Wang Yifan, Carl Doersch, Relja Arandjelović, Joao Carreira, and Andrew Zisserman. Input-level inductive biases for 3d reconstruction. In *Proceedings of the IEEE/CVF Conference on Computer Vision and Pattern Recognition*, pages 6176–6186, 2022. [3](#)
- [55] Yang Zhang, Zixiang Zhou, Philip David, Xiangyu Yue, Zelong Xi, Boqing Gong, and Hassan Foroosh. Polarnet: An improved grid representation for online lidar point clouds semantic segmentation. In *Proceedings of the IEEE/CVF Conference on Computer Vision and Pattern Recognition*, pages 9601–9610, 2020. [2](#)
- [56] Hengshuang Zhao, Li Jiang, Jiaya Jia, Philip HS Torr, and Vladlen Koltun. Point transformer. In *Proceedings of the IEEE/CVF international conference on computer vision*, pages 16259–16268, 2021. [1](#), [2](#), [6](#), [7](#)
- [57] Xinge Zhu, Hui Zhou, Tai Wang, Fangzhou Hong, Wei Li, Yuexin Ma, Hongsheng Li, Ruigang Yang, and Dahua Lin. Cylindrical and asymmetrical 3d convolution networks for lidar-based perception. *IEEE Transactions on Pattern Analysis and Machine Intelligence*, 44(10):6807–6822, 2021. [2](#)